Architecture of on- and off-axis magma bodies at EPR 9°37–40′N and implications for oceanic crustal accretion

Article *in* Earth and Planetary Science Letters · March 2014

DOI: 10.1016/j.epsl.2013.12.040

CITATIONS
10

READS
115

7 authors, including:

Shuoshuo Han
University of Texas at Austin
7 PUBLICATIONS **49** CITATIONS
SEE PROFILE

Suzanne M Carbotte
Columbia University
183 PUBLICATIONS **3,684** CITATIONS
SEE PROFILE

Omid Aghaei
Dalhousie University
14 PUBLICATIONS **60** CITATIONS
SEE PROFILE

Mladen R. Nedimović
Dalhousie University
122 PUBLICATIONS **901** CITATIONS
SEE PROFILE

Earth and Planetary Science Letters 390 (2014) 31–44

Contents lists available at ScienceDirect

Earth and Planetary Science Letters

www.elsevier.com/locate/epsl

Architecture of on- and off-axis magma bodies at EPR 9°37–40′N and implications for oceanic crustal accretion

Shuoshuo Han [a,b,*], Suzanne M. Carbotte [b], Hélène Carton [b], John C. Mutter [a,b], Omid Aghaei [c], Mladen R. Nedimović [c], J. Pablo Canales [d]

[a] Department of Earth and Environmental Sciences, Columbia University, New York, NY, USA
[b] Lamont–Doherty Earth Observatory, Palisades, NY, USA
[c] Dalhousie University, Halifax, NS, Canada
[d] Woods Hole Oceanographic Institution, Woods Hole, MA, USA

ARTICLE INFO

Article history:
Received 3 September 2013
Received in revised form 19 December 2013
Accepted 25 December 2013
Available online 20 January 2014
Editor: P. Shearer

Keywords:
off-axis magmatism
3D multi-channel seismic imaging
crustal accretion
mid-ocean ridges
East Pacific Rise
volcanism

ABSTRACT

Crustal accretion at fast-spreading mid-ocean ridges is believed to be concentrated in a narrow zone up to a few kilometers wide centered beneath the ridge axis. However, there is increasing evidence for off-axis magmatism occurring beyond this narrow zone. Here, we present 3D multichannel seismic (MCS) images from the East Pacific Rise 9°37–40′N extending to 11 km on the ridge flanks. In the axial region, two offset axial magma bodies underlie a small ridge-axis discontinuity at ~9°37′N, displaying an overlapping geometry similar to that of the seafloor structures above. On the ridge flanks, a series of off-axis magma lenses (OAML) are imaged: they are located 2–10 km from the ridge axis, at 700 to 1520 ms two-way travel time below seafloor (bsf) (~1.6 to 4.5 km bsf), with variable areas ranging from 0.5 km^2 to 5.2 km^2. The largest body is centered 4 km east of the ridge axis and is composed of a large, continuous, flat-topped lens and a series of small, discontinuous, westward-dipping bodies along its western edge. The flat crest of the OAML lies at approximately the same depth beneath layer 2A as the axial magma lens and we infer that this OAML has formed by aggregation of ascending melts that accumulate at the base of the sheeted dike section. A cluster of reflections underlying the OAML at 1260–1510 ms bsf are observed that may be deeper lenses feeding melts to the upper lens. This largest OAML is associated with Moho travel time anomalies of 120–260 ms within a zone that extends up to 2 km from the edge of the OAML, suggesting a lower crust that is partially molten with lower crustal velocities reduced by 8–18% and/or thicker than normal by up to 1 km. Local volcanic edifices are found above two of the three OAMLs imaged in our study area and are inferred to be the eruptive products of the OAMLs. From the volume of these edifices and the Moho travel time anomalies we estimate the potential contribution of off-axis magmatism to the total volume of the crust to be ~0.01–3%. The OAMLs imaged in our study area are present over roughly the same distance range as the zone of formation of near-axis seamounts. We speculate that OAMLs and the volcanic edifices found above them are small-scale manifestations of the off-axis magmatism that gives rise to near-axis seamounts.

1. Introduction

Oceanic crust is formed by decompression melting of upwelling mantle beneath mid-ocean ridges. At fast spreading ridges, although the mantle melting region beneath the ridge is several hundred kilometers wide (Forsyth et al., 1998; Key et al., 2013), new oceanic crust is believed to be generated in a narrow axial zone, where a mid-crustal melt lens about 1 km wide sits on top of a 5–7 km wide partially molten zone within the lower crust (Dunn et al., 2000; Kent et al., 1993). In places Moho can be traced to within a kilometer of the ridge axis, suggesting that the crust is fully formed at very young age (Barth and Mutter, 1996; Kent et al., 1994; Mutter and Carton, 2013). Most volcanic eruptions emanate from a narrow region a few hundreds of meters wide characterized by a small depression known as the axial summit trough (AST) and most high-temperature hydrothermal vents are located within the AST (Fornari et al., 1998; Haymon et al., 1991). For mantle melts originating from such a broad region to concentrate into the narrow crustal neovolcanic zone, strong focusing of melts within the mantle must occur.

There is however growing evidence from a number of studies conducted on fast-spreading ridges over the past two decades that mantle melts may not undergo as narrow a focusing as previously assumed. From P-to-S converted phases detected from the Moho transition zone, Garmany (1989) infers the presence of melt sills at the base of the crust about 22 km off-axis at 12°N on the East Pacific Rise (EPR). Local zones of anomalously low

* Corresponding author.

0012-821X/$ – see front matter
http://dx.doi.org/10.1016/j.epsl.2013.12.040

shear-wave velocities have been detected in seafloor compliance studies 2.5 km east of the axis at 9°08′N and 10 km east of axis at 9°48′N, indicative of a near-Moho magma lens and a low velocity zone in the lower crust, respectively (Crawford and Webb, 2002). Durant and Toomey (2009) report evidence for P-wave diffractions, P-to-S conversions, and high seismic attenuation within a region at ∼9°20′N on the EPR and located 20 km east of the axis. They attribute these observations to the presence of a melt body ∼2 km below seafloor (bsf) underlain by a low-velocity, highly attenuative crust. Lavas with anomalously young ages and diverse compositions have been sampled on the ridge flanks as far as 30 km from the ridge axis (Goldstein et al., 1994; Perfit et al., 1994; Sims et al., 2003; Turner et al., 2011; Zou et al., 2002). Hydrothermal mineral deposits indicating moderate temperature venting (up to 150 °C) have been discovered about 5 km from the ridge axis at 10°20′N (Benjamin and Haymon, 2006; Haymon et al., 2005).

In the summer of 2008, the first multi-streamer 3D multichannel seismic (MSC) survey of a mid-ocean ridge was conducted at the EPR 9°37–57′N (Mutter et al., 2009), during which a series of bright off-axis mid-crustal reflections were discovered on both flanks (Canales et al., 2012). The study of a group of these reflections at 9°52′N on the eastern flank shows that they exhibit reversed polarity with respect to the seafloor reflection, and that seismic energy propagating through the crust beneath these events is strongly attenuated (Canales et al., 2012). Based on these observations, Canales et al. (2012) conclude that these reflections are the response of off-axis magma lenses (OAML).

In this study, we analyze 3D MCS data from the southern portion of our survey extending from 9°37.6–40.0′N along the axis and to 11 km on the ridge flanks. The resulting 3D seismic images reveal the detailed geometry of the axial magma body associated with a small ridge-axis discontinuity and that of a group of OAMLs (Fig. 1). The new data show that OAMLs are abundant in the crust and form at a range of depths and distances from the axis, providing new constraints on controlling factors for the depths of crustal magma bodies. Some OAMLs are associated with Moho travel time anomalies, indicating possibly thickened crust, and volcanic cones that are likely products of eruptions from these bodies. Implications of the new observations for the potential contribution of OAMLs to overall crustal accretion, the distribution of melt on the ridge flanks, and near-axis seamount formation are considered.

2. Geological setting

The EPR 9°–10°N area is one of the most intensely studied portions of the global mid-ocean ridge system. Studies conducted over the past three decades of ridge morphology and segmentation (Macdonald et al., 1988; White et al., 2002), volcanological processes (Escartin et al., 2007; Soule et al., 2007), seismic structure of the crust and mantle (Detrick et al., 1987; Dunn et al., 2000; Toomey et al., 2007; Wilcock et al., 1995), lava geochemistry (Goss et al., 2010; Langmuir et al., 1986; Perfit et al., 1994; Rubin et al., 1994) and hydrothermal circulation (Haymon et al., 1991; Tolstoy et al., 2008) give context to our study.

The primary target of our southern survey area (Fig. 1) was a right-stepping ridge-axis discontinuity centered at 9°37′N that separates third-order ridge segments from 9°37′ to 9°20′N and 9°37′ to 9°56′N (White et al., 2006). This third-order discontinuity is expressed as a zone of overlapping ASTs extending from 9°36–38′N, with a recent history of southward propagation (Macdonald et al., 1988). The ASTs overlap by 3 km and are offset by 450 m, but no basin is developed in the overlap zone (Smith et al., 2001). Seafloor lava samples from this discontinuity show more evolved and enriched lava at the western limb, which Smith et al. (2001) attribute to waning magmatism at this retreating limb.

An early seismic study conducted in the region in 1985, during which common mid-point (CMP), wide aperture profiles (WAP), and expanded spread profile (ESP) data were acquired, provides the foundation for our modern understanding of the crustal magma plumbing system at fast spreading ridges. A cross-axis CMP profile centered at ∼9°40′N imaged an ∼700 m wide axial magma lens (AML) (Kent et al., 1993) which, based on waveform inversion studies, is largely molten (Collier and Singh, 1997; Hussenoeder et al., 1996). ESP data centered at approximately 9°35′N yield 1D velocity profiles of crust at 0, 2.1, 3.1, and 10 km from the ridge axis (corresponding to ages of 0, 38, 55, and 180 kyr, Vera et al., 1990). A tomography study conducted in 1988 covering a 20 × 20 km area from 9°27–37′N detected a 5–7 km wide low velocity zone in the mid-to-lower crust with the maximum melt fraction estimated to be ∼40% in the mid-crust (Dunn et al., 2000). This study also found a low velocity anomaly at sub-Moho depth extending to 10 km from the ridge axis that is attributed to mantle melts accumulated at the base of the crust. Regional variations in crustal thickness have been mapped from both the 1985 MCS data (Barth and Mutter, 1996) and from the later 1997 UNDERSHOOT seismic refraction study (Canales et al., 2003). Axis centered and off-axis centered mantle upwelling and melt accumulation in the shallow mantle is imaged in this region by Toomey et al. (2007). The 9°37–40′N area is at a transition from axis centered upwelling to the north to an off-axis centered mantle melt zone to the south.

3. Data and methods

3D multichannel seismic data were acquired aboard the R/V *Langseth* during cruise MGL0812 in the summer of 2008. Two groups of airguns, each composed of two gun strings with a total volume of 3300 cubic inches were towed at a nominal depth of 7.5 m and fired alternately every 37.5 m. The data were recorded with four 6-km solid-state streamers towed at a nominal depth of 10 m with 150 m spacing. Each streamer comprises 468 active hydrophone groups spaced at 12.5 m. This configuration provides a nominal bin size of 6.25 m × 37.5 m. Positions of sources and receivers were derived from shipboard and tailbuoy GPS receivers, compass-enhanced DigiCourse birds and an acoustic transponder array placed along the streamer. Data were recorded in 10-s long records with a sampling rate of 2 ms.

The data of the southern survey area used in this study were acquired along 14 across-axis primary sail lines at 300 m spacing. The resulting 3D volume (after migration) is centered at 9°38.9′N on the axis and covers an area of 4.2 km × 22.5 km (Fig. 1). In addition, one ridge-parallel 2D line (AXIS5), located 3.7 km east of the axis, is used to constrain the north–south extent of the OAML group imaged in this region. Characteristics of the OAMLs detected within the northern survey area from 9°42′N to 9°57′N (Aghaei, 2013; Canales et al., 2012; Carton et al., 2010) are also included here for comparison.

3D processing and visualization is conducted using Paradigm software Focus, GeoDepth, and VoxelGeo. The 3D pre-stack processing sequence includes 3D geometry definition (bin size 6.25 m × 37.5 m), band pass filtering (2–5–220–250 Hz) to remove cable noise, FK filtering to remove residual low frequency noise that is particularly prominent on some noisy channels and part of the line when the ship was turning, trace editing, spherical divergence correction, amplitude balancing, flexible binning, and resampling to 4 ms and 8-s trace length. Constant velocity stacks are used to determine optimal stacking velocities; the data are then normal move-out corrected and stacked with a stretch and outer mute. The post-stack processing sequence includes bottom mute of the primary seafloor multiple, 3D Kirchhoff migration with a composite velocity function modified from ESP velocity solutions

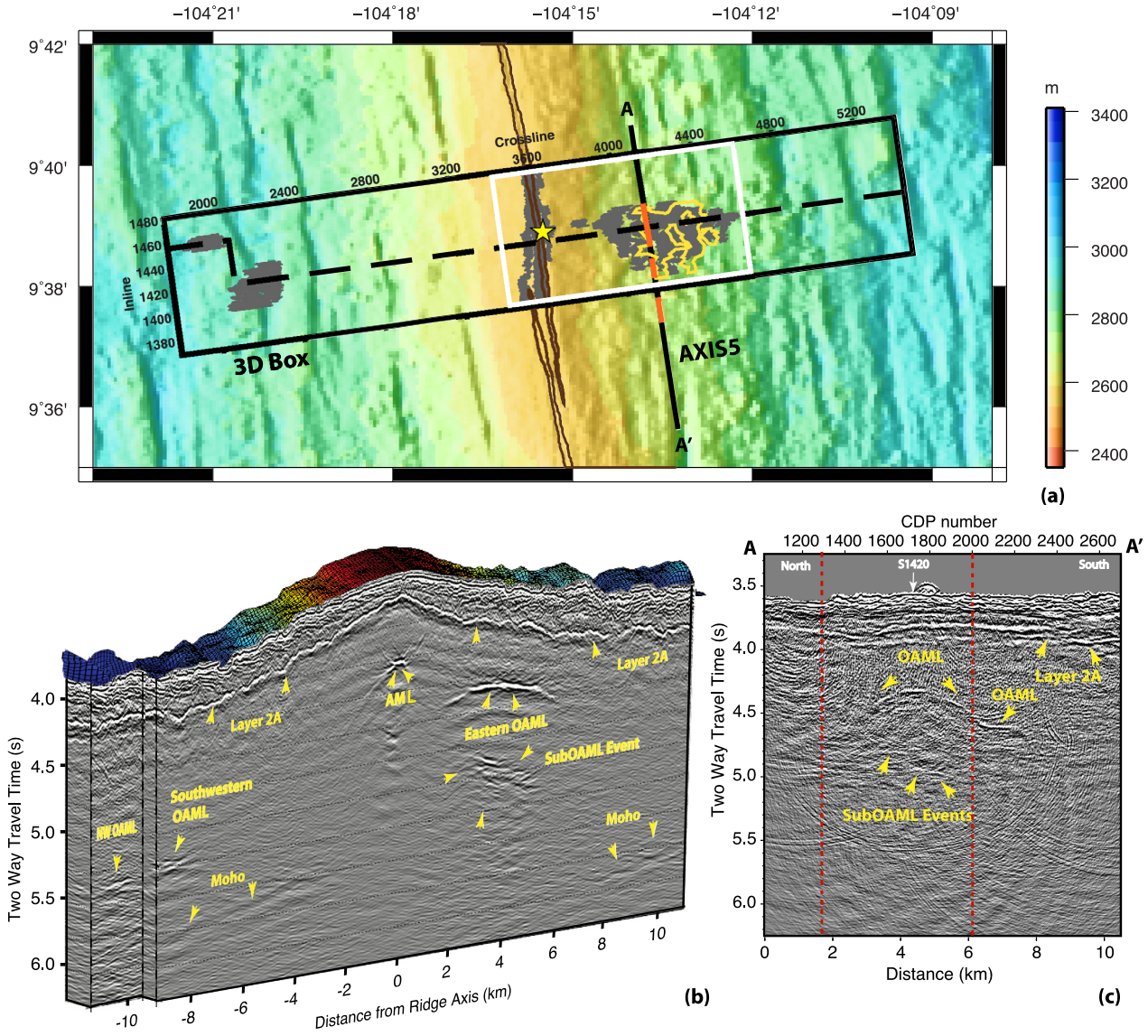

Fig. 1. Off-axis magma lens (OAML) locations within the southern 3D MCS volume (a) and representative seismic reflection cross-sections (b), (c). (a) Bathymetry of the study area. Black rectangle shows area of the 3D seismic volume with crossline and inline numbers indicated. White rectangle shows area covered in Fig. 2. Black dashed lines show the position of cut-line for view of 3D seismic volume in (b). Black line AA′ shows the position of 2D profile AXIS5 in (c). Gray shade shows area of AML and OAML; yellow line shows outline of reflections beneath the eastern OAML; orange lines on line AA′ show OAML location on AXIS5. Fine brown lines show axial summit trough from Soule et al. (2007). Yellow star indicates the location of high temperature hydrothermal vent B (Haymon et al., 1991). (b) 3D seismic image along the cut line in (a) with seismic events annotated. (c) Reflection image along AXIS5 with events annotated. Red dashed lines show the boundary of 3D volume. (For interpretation of the references to color in this figure legend, the reader is referred to the web version of this article.)

(Vera et al., 1990) and top mute above seafloor. A different volume is processed to yield the optimal image for the seismic layer 2A event. This event is stacked using source–receiver offsets from 1.3–3.7 km with velocities derived from constant velocity stacking analysis, and migrated using a 3D Kirchhoff migration algorithm. The two volumes are then merged to produce the final image. 2D processing of line AXIS5 is conducted on the data recorded by streamer 2 from both source arrays. The processing sequence is similar to that applied to the 3D data except for 2D geometry definition and 2D post-stack time migration. Seismic events identified from the composite volume (seismic layer 2A, AML, OAML and Moho) are digitized using a manually guided picking function in VoxelGeo. Uncertainties for the picked events arise from picking and stacking errors and are estimated at ±15 ms for the AML, OAML, and layer 2A event in the axial region, ±20 ms for off-axis layer 2A; and ±25 ms to ±50 ms depending on the character of the Moho reflection. Average layer 2A, layer 2B, and lower crust velocities used for depth conversion are derived from ESP profiles of Vera et al. (1990) at 9°35′N and tomography study by Canales et al. (2012) at 9°50′N.

Image resolution after migration is ∼1/8–1/4 of dominant wavelength in vertical direction and ∼1/4–1/2 of dominant wavelength in horizontal direction (Cordsen et al., 2000). One quarter of dominant wavelength at seafloor level is ∼9–11 m (assuming a dominant frequency of 35–40 Hz), at AML and OAML level is ∼40–60 m (dominant frequency 20–30 Hz), at Moho level is ∼150–220 m (dominant frequency 8–12 Hz).

4. Results

4.1. AML

Our 3D volume encompasses the northern portion of the 9°37′N ridge-axis discontinuity (Fig. 1) and reveals distinct AML reflections beneath each of the overlapping ASTs of this seafloor offset (Figs. 2 and 3(a)). The two AML events are separated laterally by 500 m, with the western AML at an average two-way travel

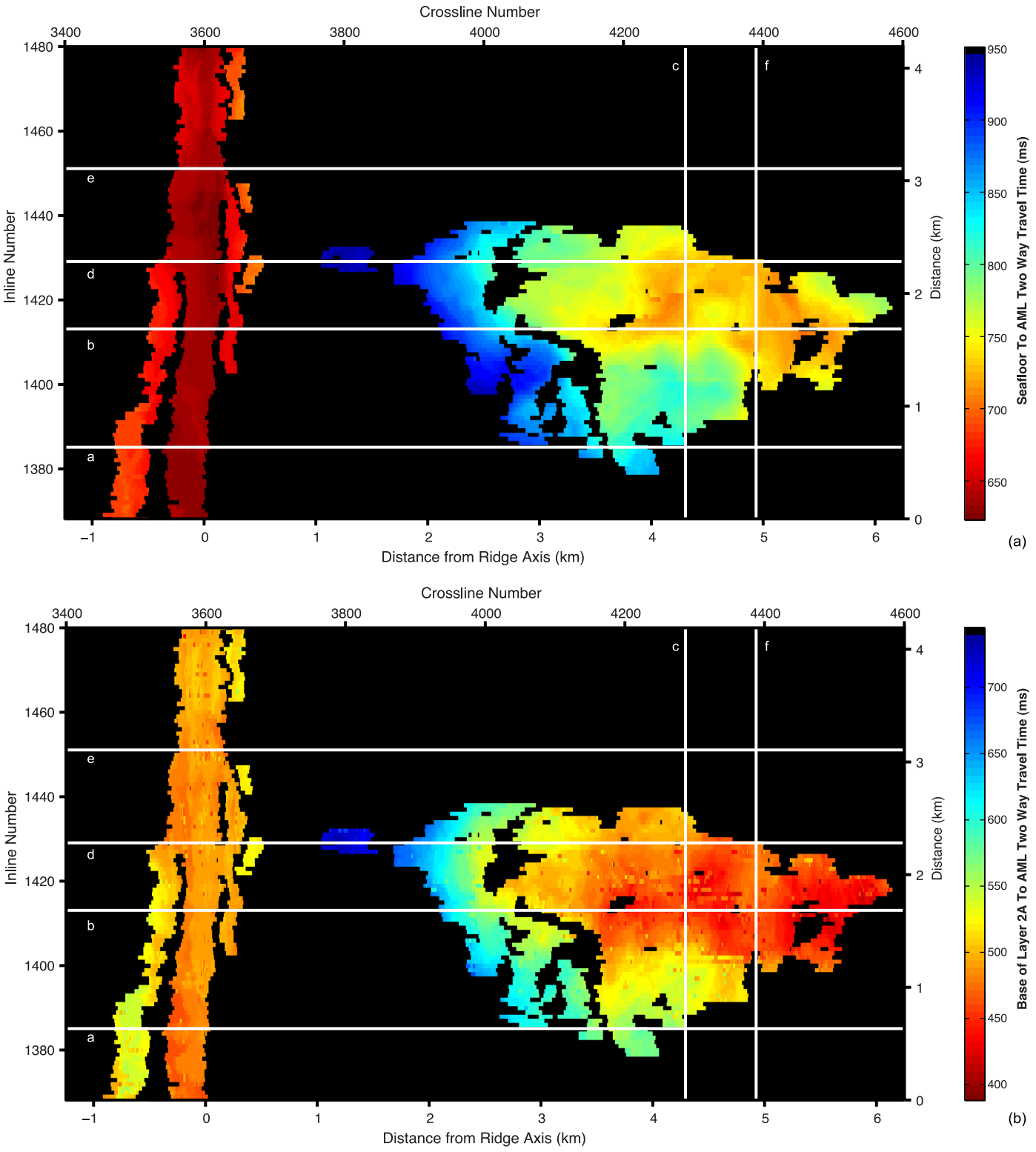

Fig. 2. Geometry of AML and OAML in map view. (a) Two-way travel time (twtt) from seafloor to AML and eastern OAML. White lines show locations of inlines/crosslines through 3D volume shown in Fig. 3. (b) Two-way travel time from the base of layer 2A to AML and eastern OAML. White lines as in (a).

time (twtt) of 690 ms bsf, ~50 ms twtt deeper than the eastern one (depth difference is ~140 m assuming average layer 2A and 2B velocity of 2.3 and 5.5 km/s respectively from ESP5, Vera et al., 1990) (Figs. 2(a) and 3(a)). The western AML reflection is ~270 m wide at the southern edge of the box and pinches out to the north at 9°38.2′N (inline 1396) (Fig. 2). The northern end of this AML extends 400 m beyond the northern tip of the western AST and is centered 100 m to the west of the AST center (Fig. 1(a)).

The AML reflection associated with the eastern AST limb lies at an average twtt of 640 ms bsf, with minor variations (±10 ms) along strike. This AML is ~320 m wide in the south where it overlaps with the western AML, increasing to 450 m in the north with the widest point (590 m) at 9°39.3′N (inline 1446). A small ~5°

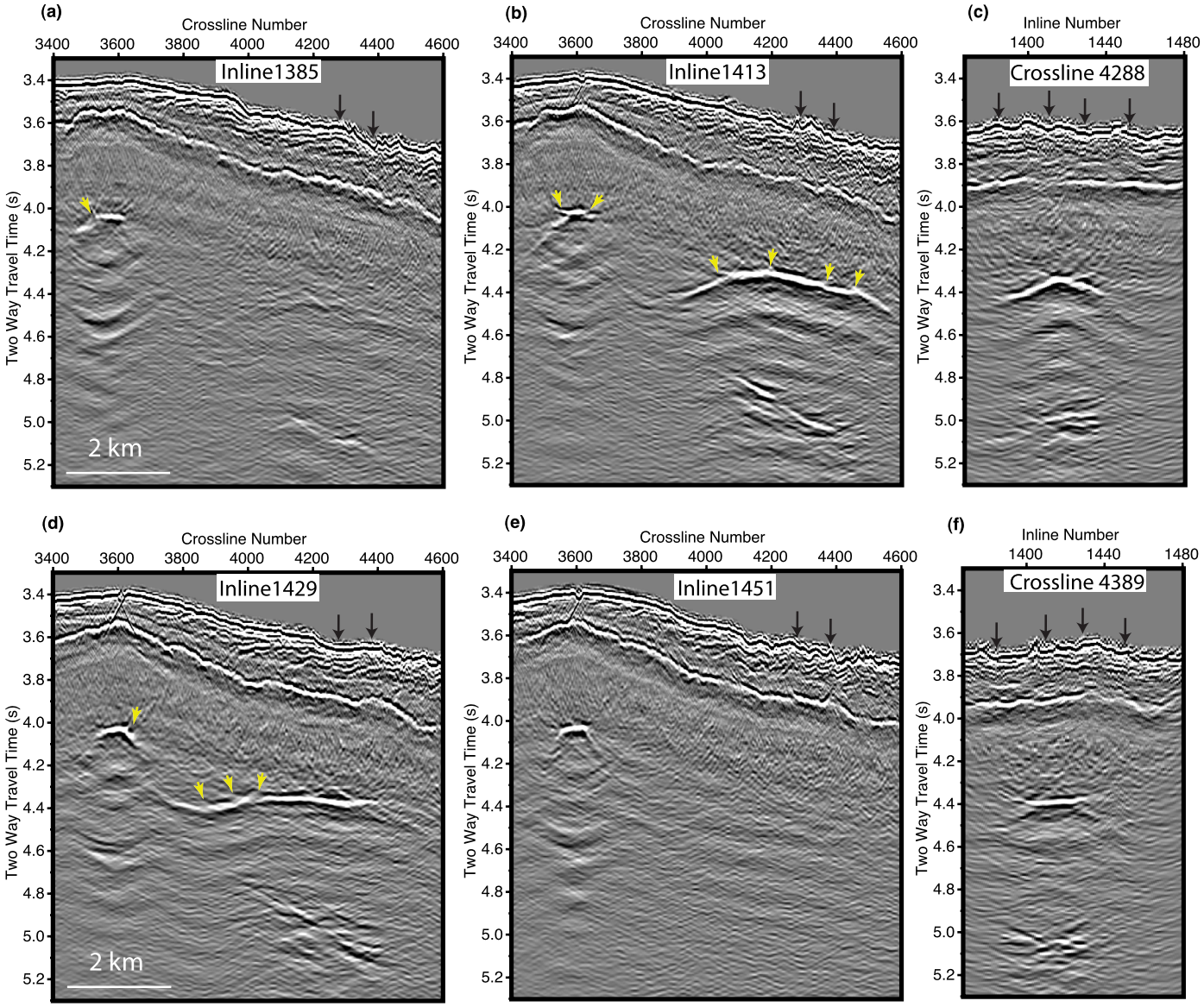

Fig. 3. Seismic images of AML and OAML in inline and crossline directions with yellow arrows indicating the interpreted boundaries between separate bodies. (a) Inline 1385: AML is a flat-lying central body with another magma body 140 m deeper and 200 m to the west. Although the OAML is faint on this inline, subevents of higher amplitude are present around 5.1 s twtt. (b) Inline 1413: AML is a flat central body with a dipping body to the west and a small magma body to the east. The OAML is dome shaped and appears to be composed of a number of smaller bodies. A cluster of bright subevents are imaged beneath the OAML with two major events that dip up to the west. (c) Crossline 4288: the OAML is dome-shaped in cross-section with a flat central part and dipping sides. Subevents form a cluster of reflectors with thickness of ~200 ms twtt. (d) Inline 1429: AML is a flat central body with a dipping event at its eastern edge. The OAML includes a small body that dips up towards the AML. Subevents are more discontinuous than in (b) and span a thicker zone of ~400 ms. (e) Inline 1451: AML is a continuous body ~600 m wide. No OAML or subevents are imaged. (f) Crossline 4389: OAML is a flat lying event. Subevents form a cluster of reflectors ~200 ms thick. (For interpretation of the references to color in this figure legend, the reader is referred to the web version of this article.)

counterclockwise change in the strike of the AML at ~9°38.9′N (inline 1430) accompanies the northward widening of this lens (Fig. 2).

On both sides of the eastern AML, small reflections that dip up towards, and in places merge with the central AML event are imaged (Figs. 2, and 3(b), (d)). These reflections extend along strike ~250–700 m and are ~120–200 m wide. These small reflections may be separate melt bodies from the main AML based on the presence of local constrictions in the reflection events with an accompanying step in travel time (Figs. 2, 3(b), (d)).

4.2. OAMLs

Away from the axial zone, the 3D seismic volume reveals bright reflections in the mid- and lower-crust on both flanks of the ridge (Fig. 1). These reflections are similar to those imaged in the northern survey area attributed to magma lenses in the off-axis crust (OAML, Canales et al., 2012). The most prominent one lies under the eastern flank, centered 4 km from the ridge axis and at 700–940 ms twtt bsf (1.6–2.4 km using off-axis layer 2A and 2B velocities of 2.3 km/s and 5.9 km/s derived from ESP1, 7, and 8 from Vera et al., 1990). This OAML reflection has a maximum span of 4.4 km in the cross-axis direction and 2.2 km in the along-axis direction, covering an area of about 5.2 km^2 (Fig. 2). Similar to the axial magma lens, the OAML reflection has reversed polarity with respect to seafloor reflection (Figs. 1(b), (c), and 3), indicating negative impedance contrast as expected for a partially molten body.

3D post-stack time migration reveals that the eastern OAML is not a continuous body but rather consists of a number of

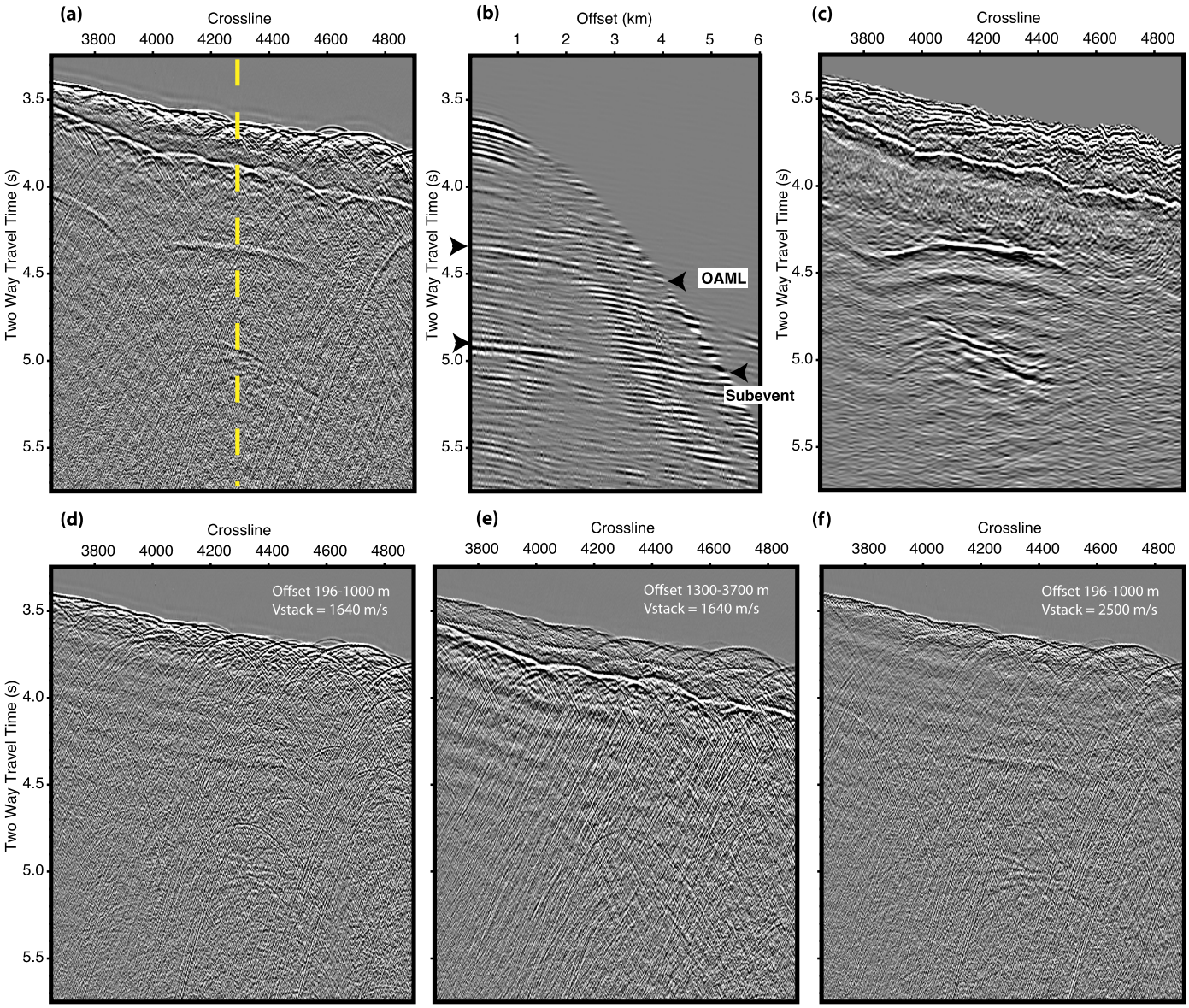

Fig. 4. Seismic characteristics of reflections beneath east flank OAML. Stacked section (a), super CMP gather that is FK filtered (b), and migrated section (c) from inline 1426 illustrating sub-OAML reflections. Yellow dash line in the stack section marks location of super CMP gather in (b). Partial offset stacks using offset range 196–1000 m and stacking velocity of 1640 m/s (d), offset range 1300–3700 m and stacking velocity of 1640 m/s (e), offset range 196–1000 m and stacking velocity of 2500 m/s (f) show that layer 2A event is not imaged at near offset, but rather imaged at middle offset, whereas both OAML event and sub-OAML event are well imaged at near-offset. (For interpretation of the references to color in this figure legend, the reader is referred to the web version of this article.)

different-size patches of high reflectivity separated by 100–450 m wide gaps (Fig. 2). The OAML is most discontinuous near its western end where a number of smaller bodies are imaged, most of which dip up to the east toward the main body. One small patch extends toward the AML around 9°39.0′N (inline 1429, Figs. 2, 3(d)), with the horizontal separation between the two of only about 900 m. At this latitude the AML also extends farthest toward east.

In the time migrated volume, the composite eastern OAML forms a dome-shaped body, elongated in the east–west direction, with an approximately flat crest in its central and eastern part (Figs. 2, 3(b)–(d), (f)). This shape is most evident after subtracting layer 2A (Fig. 2(b)) where the flat-lying region is up to 250 ms shallower than the dipping bodies of the dome rim. Velocity variations in the upper crust may contribute to these travel time variations, but are unlikely to fully account for them. If we assume an off-axis layer 2B velocity above the flat top of 5.9 km/s, lower velocities of 3.8 km/s above the OAML edges would be required to account for the greater travel time. These velocities are much slower than layer 2B velocities reported for this region from refraction studies (Christeson et al., 1996; Vera et al., 1990) and at least part of the dome shape is likely preserved in depth.

Along ridge-parallel line AXIS5, which crosses the eastern OAML 3.7 km east of the axis, another flat-lying reflection is imaged beyond the southern limit of our 3D box (Fig. 1(a), (c)). This reflection is located at 1000 ms twtt bsf, and has a north–south extent of 0.7 km (Fig. 1(c)). This body is probably part of the eastern OAML network and connects to the shallower primary body with a dipping reflection between them.

On the western flank, two smaller OAMLs are imaged (Fig. 1(a), (b)). The southwestern one is located 9 km west of the ridge axis at 1430 ms twtt bsf and covers an area of 1.7 km^2. The northwestern one is 10 km west of the ridge axis, 1520 ms twtt bsf and 0.5 km^2 in size.

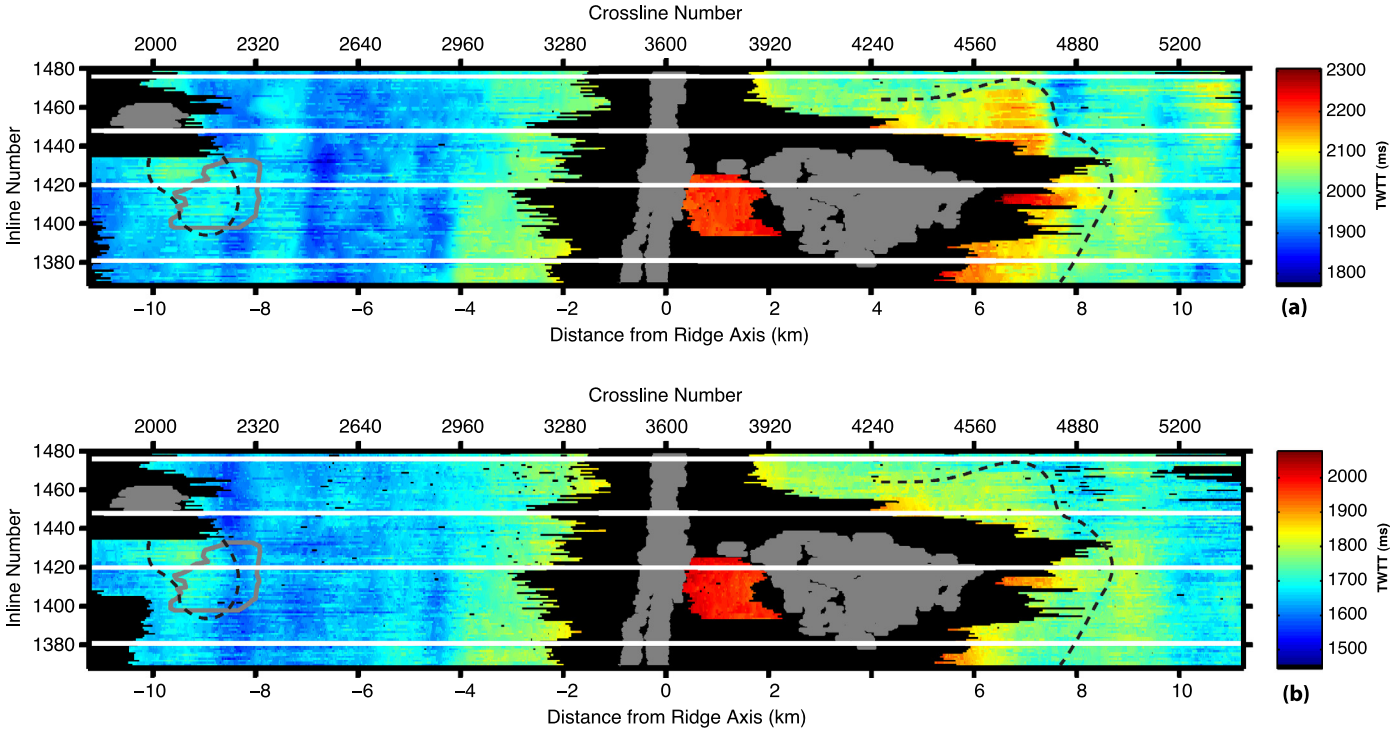

Fig. 5. Moho travel time anomalies around OAMLs. (a) Moho two-way travel time below seafloor picked from 3D volume illustrating Moho travel time anomalies near the OAMLs and ridge axis. (b) Moho two-way travel time below the base of layer 2A. White lines show locations of inlines in Fig. 6. Gray shade shows area covered by eastern OAML, northwestern OAML and AML. Grey outline shows the area covered by southwestern OAML. The weak possible Moho reflection imaged between the OAML and AML along inlines 1394–1426 has the largest travel time from seafloor. Black dashed line circles Moho travel time anomalies associated with eastern and southwestern OAMLs.

4.3. Events beneath eastern OAML

Several smaller events are imaged beneath the eastern OAML (Figs. 3(a)–(d), (f), and 4). On stack sections (Fig. 4(a)), they are evident as dipping or sub-horizontal reflections, each with identifiable diffractions. On super CMP gathers located near the center of these reflections, corresponding events extending from near to far source–receiver offsets with high velocity moveout can be identified (Fig. 4(b)). Migration velocities required to collapse diffractions from these events are slightly higher than migration velocities for the OAML above, as expected for a reflection from a deeper intracrustal body. After migration, multiple small reflections are imaged at different twtt ranging from 470–740 ms below the eastern OAML, dipping up to the west (Fig. 4(c)). They are imaged beneath the central and eastern part of the OAML and, near the southern end of the box, extend beyond the eastern end of the OAML above (Fig. 1(a)).

As for the origin of these events, converted shear arrivals from the above OAML can be ruled out as the observed events arrive ~300–400 ms later than predicted assuming the shear wave velocities for the upper crust estimated in prior studies ($V_s/V_p = 0.54$, Vera et al., 1990). These events are also unlikely to be simple inter-bed multiples. Although the average arrival time of the sub events are in the range expected for inter-bed multiples generated between the OAML and the base of layer 2A, the shape of the subevents is far more complex than that of the OAML, and does not follow the traveltime difference between the OAML and base of layer 2A. Furthermore, the subevents are evident in near-offset traces of super CMP gathers, which would not be expected for either converted shear arrivals or inter-bed multiples generated from the base of layer 2A (Fig. 4(b)). Partial offset stacks (Fig. 4(d)–(f)) show that both OAML and sub-OAML events are well imaged in the offset range of 196–1000 m, whereas the layer 2A event is imaged in the offset range of 1.3–3.7 km. Based on the above observations, we interpret the sub-OAML events as originating from true intracrustal horizons.

Similar events are observed at ~200–500 ms beneath the axial magma lens (Figs. 1, 3). A detailed analysis of the sub-AML events is presented in Marjanović (2013) using data acquired along the ridge axis. From her study, converted shear arrivals, side scatter events, and inter-bed multiples can be ruled out as possible explanations for the sub-AML events and Marjanović (2013) concludes that these events arise from magma bodies beneath the AML. We suggest a similar origin for the sub-OAML events.

4.4. Moho anomalies beneath the OAMLs

Moho reflections are generated by the impedance contrast between crustal and mantle rocks of the Moho transition zone (MTZ). For much of our study area, Moho travel times are not symmetric across the axis (Figs. 5 and 6), as would be expected for narrowly focused axis-centered accretion. On the western flank, the Moho is a sharp, high-amplitude arrival (Fig. 6). Average Moho twtt beyond the axial zone on this flank is 1940 ± 35 ms bsf (measured >4 km from the axis), increasing to ~2050 ms close to the axis. In contrast, the Moho event on the eastern flank is much more complex (Fig. 6). Moho arrivals are not detected directly beneath the OAML, and remain difficult to identify out to 0.5–0.6 km from the edge of the OAML events (Figs. 5 and 6). Within a range of ~2 km from the imaged edge of the OAML, the Moho is discontinuous, appearing as multiple arrivals at different levels, and increases in twtt toward the OAML. We use Moho traveltimes on crossline 4900–5400, located 2 km from the eastern edge of the OAML as characteristic of Moho on the eastern flank beyond the zone of influence of the OAML (average twtt is 2000 ms bsf). Relative to this flank average, the Moho twtt anomaly at the rim of OAML is ~120–260 ms (average 190 ms) (Figs. 5, 6(a), 6(b)). North of the OAML, Moho arrivals become sharper and stronger, and are more symmetric relative to the western flank (Figs. 5 and 6(d)).

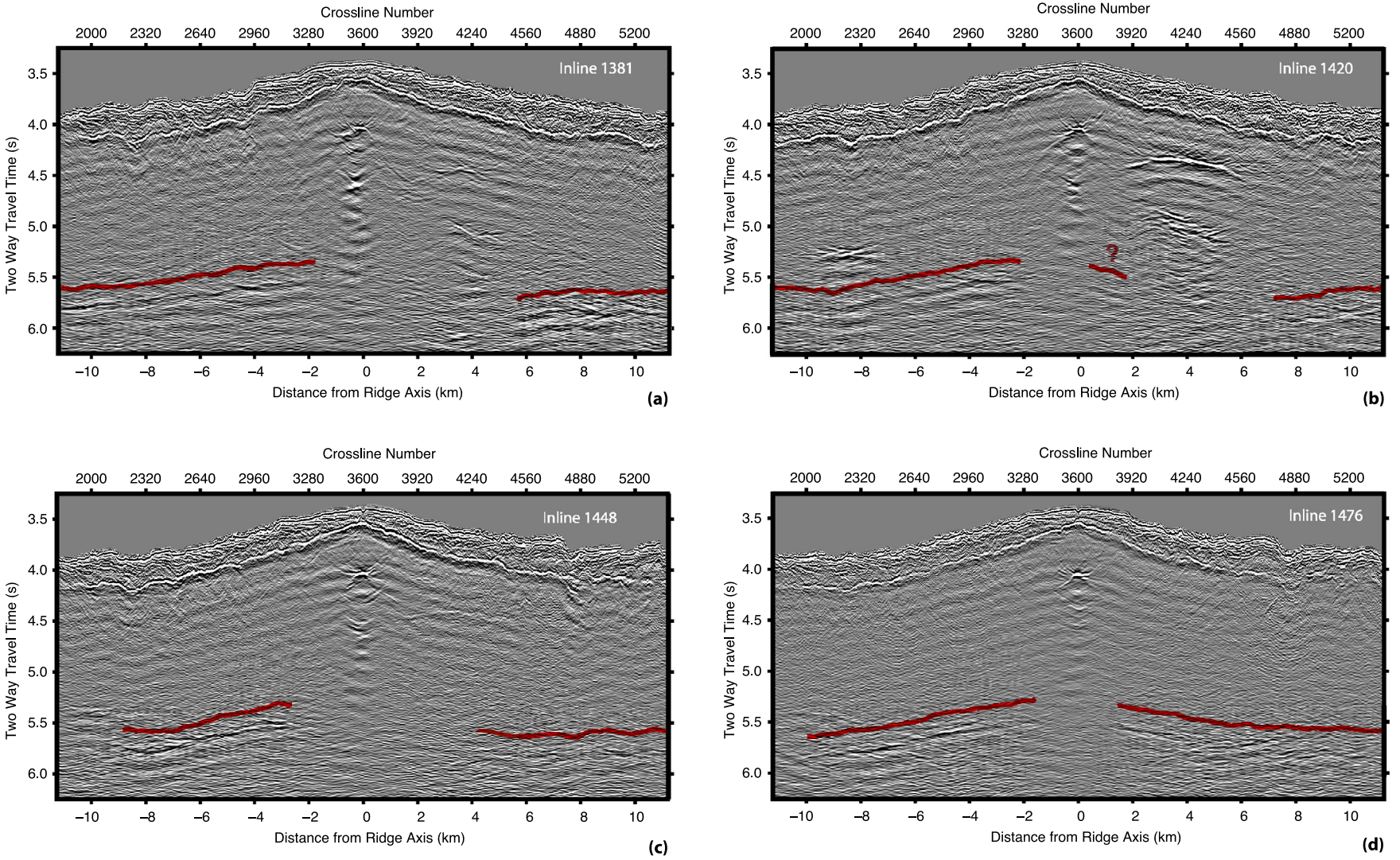

Fig. 6. Moho reflection characteristics beneath the two ridge flanks. Panels (a)–(d) show inlines 1381, 1420, 1448, 1476 respectively. Location of inlines are shown in Fig. 5. Red lines show Moho picks shifted up by 200 ms for display purpose. Where the eastern flank OAML is bright, Moho dips down towards the OAML and is a discontinuous event (inlines 1381, 1420). In contrast, Moho on the western flank dips up toward the ridge axis and is brighter and more continuous than beneath the east flank. To the north of the OAML, Moho on the eastern flank gradually becomes more symmetric (inline 1448, 1476) with the west flank Moho. (For interpretation of the references to color in this figure legend, the reader is referred to the web version of this article.)

A possible Moho reflection is imaged between the AML and the eastern OAML as a narrow, dipping reflection (Figs. 5 and 6(b)). This reflection is weak and imaged only from 9°38.4–38.9′N (inlines 1394 to 1426). It is about 150 ms deeper than Moho within similar age crust in the northern portion of the box where the OAML is absent (2080 ms). Moho is not imaged directly beneath the AML in our 3D post-stack migrated volume.

The travel time anomaly remains (although reduced in lateral extent) after removing the thickness of layer 2A, indicating it does not arise from variations in the low velocity upper crust (Fig. 5(b)). We expect that the Moho anomaly arises primarily from increased thickness and/or reduced velocities within the lower crust that extend over a broader zone than the imaged extent of the OAML. We calculate two end-member cases for the origin of the Moho travel time anomaly. If the anomaly is attributed entirely to thicker lower crust, assuming a lower crust velocity of 7.15 km/s (Vera et al., 1990), the crustal thickness anomaly is 0.4–1.0 km, 0.7 km on average. If we attribute the full travel time anomaly to anomalous lower crustal velocities instead, then the required lower crustal velocity is 5.9–6.6 km/s, about 8–18% lower than the Vera et al. (1990) estimated velocities. Determining the relative contribution of these two effects in giving rise to the observed travel time anomaly will require new observations on crustal velocities beneath the OAML, but we expect contributions from both lower velocities and thicker crust. A small Moho travel time anomaly of more limited lateral extent may also be associated with the southwestern OAML (50 ms, ∼200 m, Fig. 5).

5. Discussion

5.1. Where is the melt source for the OAML?

There are a number of possible source reservoirs to consider for the off-axis melts, including: (1) the crustal-level partial melt zone that underlies the AML; (2) the broader zone of melt accumulation at the base of the crust that feeds the ridge-axis magmatic system; and (3) local melt anomalies in the shallow mantle.

The first possibility, that the OAMLs tap melts from beneath the AML, is insufficient to explain our data. Immediately south of our study area (9°27–37′N), Dunn et al. (2000) image an axial-centered low velocity zone in the crust extending ∼3 km from the axis that they attribute to partial melt with the highest melt fraction inferred within the middle crust beneath the AML. Most of the OAMLs imaged in both our southern and northern survey areas are located beyond 3 km and up to 10 km from the ridge axis (Fig. 7). Melt delivery from the axial LVZ to feed OAML in the middle and lower crust at these distances would require extensive horizontal transport of magma beyond this zone for which there is no evidence. The geometry of the eastern OAML, with the underlying cluster of lower crustal events, suggests a system of vertically aligned magma sills at multiple levels in the crust fed by a common sub-crustal source. The plan-view shape of the OAML, with a local elongation towards the AML, does suggest possible shallow-level connectivity between the shallowest OAML and the AML in both the southern (Figs. 3(d) and 7) and northern (Canales et al., 2012) survey areas. However, given the expected buoyancy of melt in the crust, it is more likely that the melt in the OAML migrates uphill toward the axial crustal reservoir than that the AML feeds melt laterally to deeper levels in the off-axis crust.

The zone of melt accumulation at the base of the crust beneath the EPR detected in prior seismic and compliance studies is ∼10–20 km wide, with an estimated melt fraction of 3–11%, possibly distributed in local sills within and beneath the MTZ (Crawford and Webb, 2002; Dunn et al., 2000; Garmany, 1989; Toomey et al., 2007). The off-axis extent of this partial melt zone is comparable to the distance over which OAMLs are observed in both our northern (Canales et al., 2012) and southern study areas and the OAMLs may result from local tapping of this broad sub-crustal reservoir on the ridge flanks. The development of this melt reservoir is attributed to the presence of permeability barriers at the base of the axial lithosphere, possibly due to rapid crystallization of plagioclase and clinopyroxene (Kelemen and Aharonov, 1998). Local topography at the base of the lithosphere may facilitate thermal or melt erosion of this boundary; tensile fracture caused by bending-related stress (Sohn and Sims, 2005) may also create pathways for over-pressured sub-Moho melt to intrude into the off-axis crust and form OAMLs.

Another possibility we consider is that the OAMLs reflect the presence of small local melt anomalies in the shallowest mantle. Long-term chemical heterogeneities in the mantle are believed to exist at different length scales (e.g. Fornari et al., 1988; Niu and Batiza, 1997; Zindler and Hart, 1986. These heterogeneous blobs may begin to melt at different depths and segregate from the main melt focusing zone, bypassing delivery to the axis. In the recent numerical modeling study of Katz and Weatherley (2012), preferentially melted heterogeneities can nucleate high porosity, high permeability channels for rapid magma ascent. Melt segregation from this heterogeneous mantle source may create localized zones of trapped melt at the base of the lithospheric boundary layer, which may deliver melt via dikes or channels to the off-axis crust. Melt from these small anomalies could contribute to the broad subcrustal low velocity zone imaged in seismic studies. However, the chemical composition of these melts may be distinguished from an NMORB source. Enriched MORB, indicating the presence of local mantle heterogeneities, are sampled in the EPR 9°–10°N region, but exclusively on the ridge flanks (>0.5 km from ridge axis, Perfit et al., 1994; Sims et al., 2003; Smith et al., 2001; Waters et al., 2011). While some studies favor an off-axis source for these lavas (Goldstein et al., 1994; Perfit et al., 1994), others suggest EMORB are erupted in the axial zone and then are transported several kilometers off-axis through lava tubes and/or via surface channels (Sims et al., 2003; Waters et al., 2011). Our study shows that off-axis magma bodies do exist in this area that could be the source of the EMORB sampled in this region. Future sampling studies of lavas above the OAMLs imaged here will be needed to clarify the relationships between E-MORB and off-axis magmatism.

5.2. What controls the depth of OAMLs?

Melt ascent in magmatic systems is driven primarily by the buoyancy of melt with respect to the surrounding country rock. However, the mechanisms by which melts stall and form sills are not well understood. A number of mechanisms have been proposed for sill formation including melt ponding due to the presence of a freezing front (Phipps Morgan and Chen, 1993) or a rheological boundary (e.g. Parsons et al., 1992), both of which are fundamentally linked to the regional thermal structure. Other mechanisms include the presence of a rigidity contrast between elastic layers where sills form at an interface between weak and strong layers (e.g. Menand, 2008), or changes in the local stress regime where the least compressive stress becomes vertical due to dike intrusion (Gudmundsson, 1990). At mid-ocean ridges, the regionally-averaged depth of the AML increases with decreasing spreading rate, consistent with thermal models of crustal accretion (Henstock et al., 1993; Phipps Morgan and Chen, 1993). It is commonly believed that axial thermal structure plays a key role in the depth at which the AML resides in the crust. The OAMLs mapped here and within the northern survey area (Aghaei, 2013) reside at a range of depths within the crust. To assess what factors control the depths of OAMLs, we examine their depth distribution on the ridge flanks in light of existing thermal models.

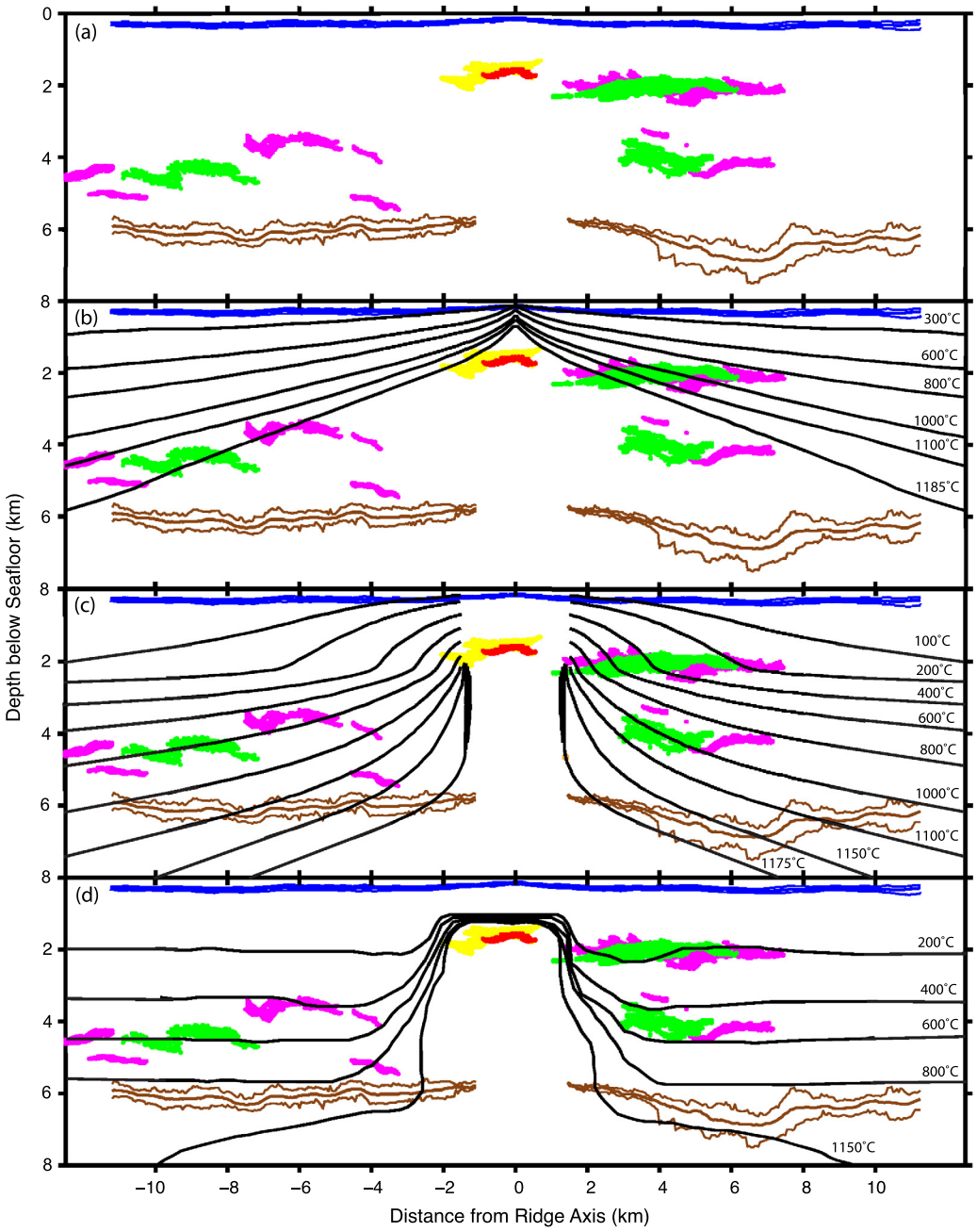

Fig. 7. AML and OAML picks from both the southern and northern 3D volumes superimposed onto a single cross-section and converted to depth (see text). Axial and off-axis magma lens depths are compared with predicted isotherms from three ridge axis thermal models from; (b) Sleep (1975), (c) Henstock et al. (1993), and (d) Dunn et al. (2000). Red shade and green shade are the AML and OAML picks from the southern 3D box analyzed in this study. Yellow shade and pink shade are AML (Carton et al., 2010) and OAML (Aghaei, 2013) picks from the northern 3D volume. Blue bold line shows the average layer 2A position in this 3D box with fine blue lines showing the range of layer 2A depth. Brown bold line shows the average Moho position in this 3D box with fine brown lines showing the range of Moho depths (the possible Moho reflection between AML and eastern OAML is not included in this average). The black lines are isotherms of each thermal model. (For interpretation of the references to color in this figure legend, the reader is referred to the web version of this article.)

Two-way travel times to all OAMLs imaged in both the southern and northern 3D survey areas are converted to depth below seafloor (Fig. 7(a)) using the cross-axis velocity profile from Canales et al. (2012) at 9°50′N. All OAMLs are superimposed on a composite vertical section and compared with three different thermal models for this fast spreading ridge (Dunn et al., 2000; Henstock et al., 1993; Sleep, 1975). The model of Sleep (1975) ignores the effects of hydrothermal circulation and represents the hot end-member thermal model (Fig. 7(b)). The model of Henstock et al. (1993), like that of Phipps Morgan and Chen (1993), includes hydrothermal circulation modeled as enhanced conductive cooling in the upper crust (Fig. 7(c)). The thermal model of Dunn et al. (2000) is derived from their P-wave velocity model for the 9°27–37′N area (calculated to include effects of anelasticity, Fig. 7(d)). Predicted temperatures in the crust beyond ∼4 km from the ridge axis are colder for this model than the others, and hence the Dunn et al. (2000) model represents the coldest ridge flank end member of the models considered.

Of all the OAMLs shown on the composite section (Fig. 7), the most prominent ones are also the shallowest and the closest to the ridge axis. It is striking that in both northern and southern survey areas the most prominent OAMLs are located at almost the same depth, at the same distance from the axis, and with similar east–west extents (Fig. 7(a)), and lie only ∼200 m bsf deeper than

the nearby axial magma lens. Considering that the thickness of layer 2A increases by 200–300 m from the axis to off-axis region, we hypothesize that these two major OAMLs reside at the base of the sheeted dikes. These shallowest OAMLs are located within cold crustal regions predicted by all ridge thermal models. However, our study and that of Canales et al. (2012) show that there is evidence for zones of higher melt fraction and/or high temperatures in the lower crust beneath these bodies. No significant zone of low velocities/thicker crust is detected beneath the other small OAMLs imaged by our study. In fact significant melt volumes in the lower crust may be required to generate OAMLs that can rise to the base of sheeted dikes. We speculate that permeability barriers at the dike/gabbro transition associated with the AML are preserved off-axis and provide barriers to melts rising in the off-axis environment. Hence, the depths of these shallowest OAMLs could be governed primarily by this inherited lithologic contrast, rather than by ridge flank thermal structure.

Most of the remaining OAMLs located outside of the axial LVZ lie at 3–5 km bsf, with deeper events located further from the ridge axis. These OAMLs align roughly with the 1000–1200 °C isotherms of the Sleep (1975) model (Fig. 7(b)), which correspond to the solidus for basaltic melts. As with the AML, the implication is that the deeper OAMLs stop at a freezing front where the dilatational volume change associated with magma freezing leads to viscous stresses that favor magma ponding (Phipps Morgan and Chen, 1993). However, the Sleep (1975) thermal model implies that, as in the axial zone, crust beneath these OAMLs should be partially molten, which is inconsistent with existing seismic observations in the region (Vera et al., 1990; Dunn et al., 2000). In the Henstock et al. (1993) thermal model (Fig. 7(c)), the deeper OAMLs align with the 600–800 °C isotherms, which is in the range of temperatures for the brittle–ductile transition. In this case, the rheological contrast between ductile lower crust and brittle rock above would provide a barrier to feeder dikes and promote sill formation (Menand, 2011; Parsons et al., 1992). We favor the explanation that the brittle–ductile transition zone contributes to the formation of the deeper OAMLs. This barrier may be sufficient to trap off-axis melts with small and ephemeral sources. Perhaps only off-axis crustal melts with larger and longer-lived source reservoirs can breach this barrier and rise to shallower levels, like the most prominent OAMLs in both northern and southern survey areas. In the Dunn et al. (2000) thermal model (Fig. 7(d)), most OAMLs lie in cold crust <600 °C where melt bodies would be predicted to rapidly freeze. From this, we speculate that the Dunn et al. (2000) thermal model is inconsistent with the abundance of OAML imaged in our study.

5.3. How abundant are OAMLs and how much do they contribute to crustal accretion?

Within the full extent of our 3D MCS survey, 11 OAMLs are imaged covering a total area of 23.7 km^2 equivalent to about 3% of the survey area. This area is comparable to that encompassed by the AML of 23.8 km^2. The observations from our survey indicate that OAMLs are abundant and may be common at fast spreading ridges.

Given the observed abundance of OAML, how much do they contribute to the total crustal volume? We address this question by assessing both the potential extrusive and intrusive contribution. Volcanic edifices are observed above the eastern and southwestern OAMLs in our study area. Above the eastern OAML, a series of four small cones are found, oriented parallel to the spreading direction and extending for 2.4 km (Fig. 8(a)–(d)). The westernmost cone is the largest, ~60 m tall and 800 m in diameter. The other three cones are 30–40 m tall (Fig. 8(d)). The estimated volume of this group of volcanic edifices is 4.48×10^7 m^3. This estimate is a minimum for the extrusive volume associated with this cluster of volcanic cones, given that the likely contribution of lavas covering adjacent seafloor and channeled within nearby grabens (Fig. 8(a)) is not considered.

The elongation of this set of volcanic cones in the direction of spreading indicates either sustained eruption from a common source at the western edge of the OAML or simultaneous eruptions from multiple points aligned along a ridge-perpendicular trend. For the former case, at a half spreading rate of 56 mm/yr, the length of the volcanic cone field indicates duration of eruptive activity of 43 kyr. The largest cone is located above the patchy western edge of the OAML (Fig. 8(b)). This patchy region consists of several small bodies that dip up toward the shallow flat-topped portion of the OAML, suggestive of active magma delivery from below. Eruptions may occur preferentially in this region of higher magma supply (Menand, 2011). We interpret the large and more continuous sill to the east as the result of the aggregation of smaller melt bodies that rise vertically and pool at the base of the dike section.

The southwestern OAML is located beneath an ~50 m deep and 0.6–1.3 km wide graben (Fig. 8(e)–(g)). A small volcanic cone with a volume of 2.14×10^7 m^3 fills the graben immediately above the southwest OAML and is assumed to have erupted from this body. The total volume of the volcanic edifices associated with both the southwestern and eastern OAML is 6.62×10^7 m^3, which represents ~0.25% of the total extrusive volume and ~0.01% of the total crustal volume within our southern 3D survey area.

The intrusive contribution of the imaged OAML to crustal accretion is estimated from the Moho travel time anomalies associated with these features. The eastern OAML is associated with a Moho travel time anomaly, which if attributed entirely to thickened crust, indicates an average crustal thickness anomaly of 700 m. Assuming this anomaly for the area affected by the OAML, the total volume of added crust is 16.7 km^3, corresponding to 2.9% of the crustal volume within our study area. The southwestern OAML is associated with a modest travel time anomaly that is not significantly above our picking error and Moho is not imaged beneath the northwestern OAML (Fig. 5). Therefore the intrusive contribution of the OAMLs is calculated solely from the eastern OAML. If the Moho anomaly associated with this feature is due not to thickened crust but rather slower velocities, then the intrusive contribution is negligible. Combining estimates of both the extrusive and intrusive volume associated with the OAMLs, the total contribution to crustal accretion within our survey area is ~0.01–3%. We conclude that although OAMLs are abundant in the young crust at this fast spreading ridge, their contribution to the volume of oceanic crust is small.

We acknowledge that our 3D MCS image provides only a snapshot of the dynamic mid-ocean ridge environment and many more OAMLs are likely to have existed in the past within this region. Once cooled and solidified, these bodies would be indistinguishable from the surrounding crust unless they are associated with significant crustal thickness anomalies. Based on crustal thickness data from our southern (this study) and northern (Aghaei, 2013) survey areas, there is evidence for small localized crustal thickness anomalies that may be attributed to ancient OAMLs, but there are no sizable anomalies comparable to the eastern OAML in the southern box. Our data suggest a spectrum of sizes and longevities for the OAMLs and variable individual contributions. The main OAML in our southern survey area was detected as an “intracrustal reflector” in MCS data acquired in 1985 (CMP line 559, Barth and Mutter, 1996) and clearly has existed for at least 23 yr. The string of volcanic constructs above and the evidence for the thicker crust and/or lower crustal velocities below suggest that it has likely existed much longer and is fed by a significant underlying melt source reservoir. OAMLs of this type may influence local crustal

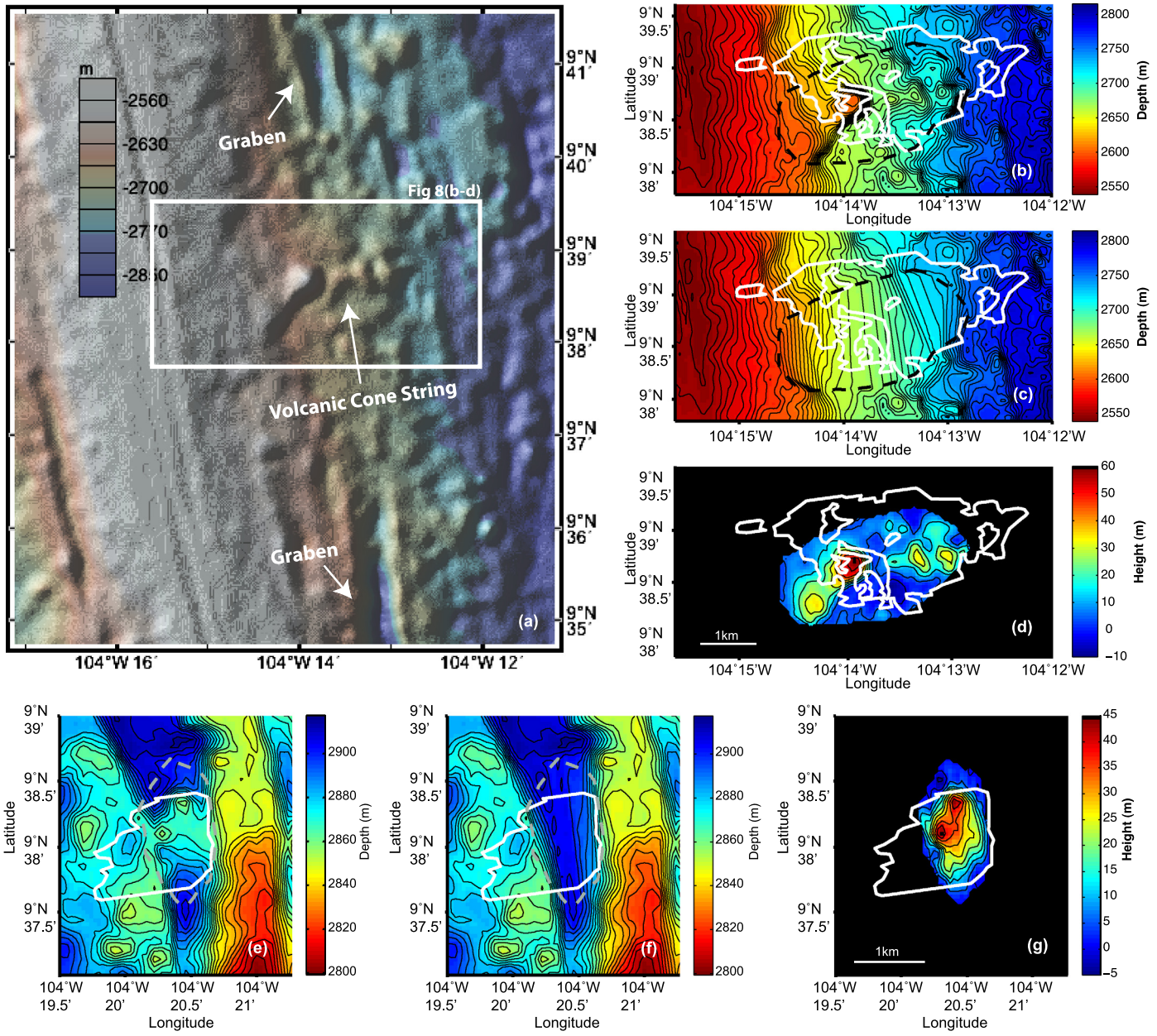

Fig. 8. Estimation of volume of volcanic structures interpreted to have erupted from OAMLs. (a) Bathymetry of the eastern ridge flank (vertical exaggeration = 5) shows the volcanic cone string above the eastern OAML. The graben to the north and south is likely filled by lava erupted from the OAML. (b) Seafloor bathymetry in the white rectangular in panel (a); white solid line shows the plan view extent of the underlying OAML. Volcanic edifice in area enclosed in black dashed line is isolated for volume estimation. (c) The bathymetry within the black dashed line is nulled; and the bathymetry outside the black dashed line is interpolated to give the background bathymetry of this area. (d) Isolated topography for the volcanic edifices above the eastern OAML calculated by subtracting the background bathymetry from original bathymetry. (e)–(g) Same as panels (b)–(d) above for southwestern OAMLs. (For interpretation of the references to color in this figure legend, the reader is referred to the web version of this article.)

structure and thickness orders of magnitude more than the small OAMLs.

5.4. How are OAMLs related to near-axis seamount formation?

Near-axis seamounts are abundant on the flanks of fast-spreading ridges (Alexander and Macdonald, 1996; Batiza, 2001; Scheirer and Macdonald, 1995; Shen et al., 1993; White et al., 1998). They are typically several tens to hundreds of meters tall; they often align in small chains, and are believed to form 5–15 km from the ridge axis. Although they cover about 13–17% of the seafloor, they are estimated to contribute only a few percent to the volume of oceanic crust (Alexander and Macdonald, 1996; Scheirer and Macdonald, 1995; Shen et al., 1993). Geochemical studies of lavas from these near-axis seamounts indicate they share the same mantle source as lavas erupted at the ridge axis (Fornari et al., 1988; Zindler et al., 1984). However, their chemical composition is much more diverse than that of axial lavas, varying from extremely depleted tholeiites to highly enriched alkali basalts (Niu and Batiza, 1997; Niu et al., 2002). This compositional variation is believed to reflect small-scale heterogeneity in the mantle source (Donnelly et al., 2004; Niu et al., 2002). Near-axis seamount lavas are also typically more primitive than axial lavas, an observation attributed to short residence times in crustal magma chambers (Batiza et al., 1990; Fornari et al., 1988).

The OAMLs imaged in our study area are present over roughly the same distance range as the formation zone for near-axis seamounts. Small volcanic edifices are observed above OAMLs, indicating OAMLs can give rise to volcanic construction on the seafloor. Furthermore, the spreading-direction parallel elongation of the series of volcanic constructs above the eastern OAML is analogous to that of near-axis seamount chains and suggests a local zone of off-axis melt delivery that persists with ongoing seafloor spreading. Given these similarities, we speculate that OAMLs are small-scale manifestations of the off-axis magmatism that gives rise to near-axis seamounts. The lavas erupted from OAMLs may represent the youngest products of seamount volcanism and sampling these lavas could provide information on of the subcrustal mantle melt reservoir that leads to seamount formation.

6. Conclusions

3D MCS imaging of the EPR reveals abundant magma lenses on the flanks of this fast-spreading ridge, present at a range of depths within the crust and of varying size. OAMLs are detected at distances up to 10 km from the ridge axis well beyond the axial zone of presumed high melt content, and we conclude that melt pathways to the OAMLs from the uppermost mantle melt reservoir are separate from those feeding the AML. A cluster of reflections are imaged beneath the most prominent OAML at 9°39′N which are likely deeper magma sills, suggesting a system of magma sills at multiple levels fed by a common sub-crustal source. Small dipping bodies are imaged at the edges of both the OAML and the AML. It is thus likely that these crustal magma lenses form by aggregation of smaller magma bodies that ascend from depth and pond at shallower permeability barriers.

The largest OAMLs found in our study area reside at depths consistent with accumulation at the base of the sheeted dike section. We hypothesize that the gabbro-to-dike lithologic transition, which forms in the axial zone, remains a major permeability barrier to melts rising in the off-axis environment. These OAMLs are also associated with Moho travel time anomalies and in the northern survey area zones of high attenuation in the lower crust, suggesting significant melt volumes, elevated temperatures, and/or increased crustal thickness. Other smaller OAML are located deeper in the crust but mostly at shallower depths than the predicted freezing horizon for gabbro derived from existing ridge thermal models. These OAMLs may form at rheological or compositional barriers within the gabbro section. Local melt anomalies within the uppermost mantle that can deliver significant melt volumes to the lower crust may be required to produce OAMLs that can breach these barriers in the gabbro section, rise up and pond at the base of the sheeted dikes.

Although the OAMLs are abundant, estimates from this study indicate they only contribute a few percent in overall crustal volume. While some OAMLs appear to have a persistent source that may supply melts to the crust for thousands of years, many OAMLs likely have small and ephemeral sources that do not support prolonged intrusion. The small volume contribution of the OAMLs leads us to conclude that in general, melt focusing in the mantle beneath fast-spreading ridges is efficient. However, effects of off-axis magmatism on other crustal properties may be significant: intrusion of OAMLs are expected to modify the thermal structure, mineralogy and composition of the surrounding country rock, and may facilitate high temperature off-axis hydrothermal circulation on the ridge flanks well away from the axial zone.

Acknowledgements

We thank the *R/V M.G. Langseth's* Captain M. Landow, crew, and technical staff led by R. Steinhaus for their efforts, which made possible the success of cruise MGL0812. We thank Peter B. Kelemen, Spahr C. Webb, and W. Roger Buck for their insightful discussions. This research is funded by US National Science Foundation.

References

Aghaei, O., 2013. The East Pacific Rise crustal thickness, Moho Transition Zone character and off-axis magma lens melt content from 9°37.5′N to 9°57′N: results from three-dimensional multichannel seismic data analysis. Dalhousie University, Halifax, Nova Scotia, Canada.

Alexander, R.T., Macdonald, K.C., 1996. Small off-axis volcanoes on the East Pacific Rise. Earth Planet. Sci. Lett. 139, 387–394.

Barth, G.A., Mutter, J.C., 1996. Variability in oceanic crustal thickness and structure: Multichannel seismic reflection results from the northern East Pacific Rise. J. Geophys. Res., Solid Earth 101, 17951–17975.

Batiza, R., 2001. Seamounts and off-ridge volcanism. In: John, H.S. (Ed.), Encyclopedia of Ocean Sciences. Academic Press, Oxford, pp. 2696–2708.

Batiza, R., Niu, Y.L., Zayac, W.C., 1990. Chemistry of seamounts near the East Pacific Rise – Implications for the geometry of subaxial mantle flow. Geology 18, 1122–1125.

Benjamin, S.B., Haymon, R.M., 2006. Hydrothermal mineral deposits and fossil biota from a young (0.1 Ma) abyssal hill on the flank of the fast spreading East Pacific Rise: Evidence for pulsed hydrothermal flow and tectonic tapping of axial heat and fluids. Geochem. Geophys. Geosyst. 7.

Canales, J.P., Detrick, R.S., Toomey, D.R., Wilcock, W.S.D., 2003. Segment-scale variations in the crustal structure of 150–300 kyr old fast spreading oceanic crust (East Pacific Rise, 8°15′N–10°5′N) from wide-angle seismic refraction profiles. Geophys. J. Int. 152, 766–794.

Canales, J.P., Carton, H., Carbotte, S.M., Mutter, J.C., Nedimovic, M.R., Xu, M., Aghaei, O., Marjanovic, M., Newman, K., 2012. Network of off-axis melt bodies at the East Pacific Rise. Nat. Geosci. 5, 279–283.

Carton, H., Carbotte, S.M., Mutter, J.C., Canales, J.P., Nedimovic, M.R., Aghaei, O., Marjanovic, M., Newman, K., 2010. Three-dimensional seismic reflection images of axial melt lens and seismic Layer 2A between 9°42′N and 9°57′N on the East Pacific Rise. Eos, Trans. Am. Geophys. Union 90.

Christeson, G.L., Kent, G.M., Purdy, G.M., Detrick, R.S., 1996. Extrusive thickness variability at the East Pacific rise, 9°–10°N: Constraints from seismic techniques. J. Geophys. Res., Solid Earth 101, 2859–2873.

Collier, J.S., Singh, S.C., 1997. Detailed structure of the top of the melt body beneath the East Pacific Rise at 9°40′N from waveform inversion of seismic reflection data. J. Geophys. Res., Solid Earth 102, 20287–20304.

Cordsen, A., Galbraith, M., Peirce, J., 2000. Planning Land 3-D Seismic Surveys. Society of Exploration Geophysicists, Tulsa.

Crawford, W.C., Webb, S.C., 2002. Variations in the distribution of magma in the lower crust and at the Moho beneath the East Pacific Rise at 9°–10°N. Earth Planet. Sci. Lett. 203, 117–130.

Detrick, R.S., Buhl, P., Vera, E., Mutter, J., Orcutt, J., Madsen, J., Brocher, T., 1987. Multichannel seismic imaging of a crustal magma chamber along the East Pacific Rise. Nature 326, 35–41.

Donnelly, K.E., Goldstein, S.L., Langmuir, C.H., Spiegelman, M., 2004. Origin of enriched ocean ridge basalts and implications for mantle dynamics. Earth Planet. Sci. Lett. 226, 347–366.

Dunn, R.A., Toomey, D.R., Solomon, S.C., 2000. Three-dimensional seismic structure and physical properties of the cust and shallow mantle beneath the East Pacific Rise at 9°30′N. J. Geophys. Res., Solid Earth 105, 23537–23555.

Durant, D.T., Toomey, D.R., 2009. Evidence and implications of crustal magmatism on the flanks of the East Pacific Rise. Earth Planet. Sci. Lett. 287, 130–136.

Escartin, J., Soule, S.A., Fornari, D.J., Tivey, M.A., Schouten, H., Perfit, M.R., 2007. Interplay between faults and lava flows in construction of the upper oceanic crust: The East Pacific Rise crest 9°25′–9°58′N. Geochem. Geophys. Geosyst. 8.

Fornari, D.J., Perfit, M.R., Allan, J.F., Batiza, R., 1988. Small-scale heterogeneities in depleted mantle sources – near-ridge seamount lava geochemistry and implications for mid-ocean-ridge magmatic processes. Nature 331, 511–513.

Fornari, D.J., Haymon, R.M., Perfit, M.R., Gregg, T.K.P., Edwards, M.H., 1998. Axial summit trough of the east Pacific rise 9°–10°N: Geological characteristics and evolution of the axial zone on fast spreading mid-ocean ridges. J. Geophys. Res., Solid Earth 103, 9827–9855.

Forsyth, D.W., Scheirer, D.S., Webb, S.C., Dorman, L.M., Orcutt, J.A., Harding, A.J., Blackman, D.K., Morgan, J.P., Detrick, R.S., Shen, Y., Wolfe, C.J., Canales, J.P., Toomey, D.R., Sheehan, A.F., Solomon, S.C., Wilcock, W.S.D., Team, M.S., 1998. Imaging the deep seismic structure beneath a mid-ocean ridge: The MELT experiment. Science 280, 1215–1218.

Garmany, J., 1989. Accumulations of melt at the base of young oceanic-crust. Nature 340, 628–632.

Goldstein, S.J., Perfit, M.R., Batiza, R., Fornari, D.J., Murrell, M.T., 1994. Off-axis volcanism at the East Pacific Rise detected by uranium-series dating of basalts. Nature 367, 157–159.

Goss, A.R., Perfit, M.R., Ridley, W.I., Rubin, K.H., Kamenov, G.D., Soule, S.A., Fundis, A., Fornari, D.J., 2010. Geochemistry of lavas from the 2005–2006 eruption

at the East Pacific Rise, 9°46′N–9°56′N: Implications for ridge crest plumbing and decadal changes in magma chamber compositions. Geochem. Geophys. Geosyst. 11.
Gudmundsson, A., 1990. Emplacement of dikes, sills and crustal magma chambers at divergent plate boundaries. Tectonophysics 176, 257–275.
Haymon, R.M., Fornari, D.J., Edwards, M.H., Carbotte, S., Wright, D., Macdonald, K.C., 1991. Hydrothermal vent distribution along the East Pacific Rise crest (9°09′–54′N) and its relationship to magmatic and tectonic processes on fast-spreading mid-ocean ridges. Earth Planet. Sci. Lett. 104, 513–534.
Haymon, R.M., McDonald, K.C., Benjamin, S.B., Ehrhardt, C.J., 2005. Manifestations of hydrothermal discharge from young abyssal hills on the fast-spreading East Pacific Rise flank. Geology 33, 153–156.
Henstock, T.J., Woods, A.W., White, R.S., 1993. The accretion of oceanic-crust by episodic sill intrusion. J. Geophys. Res., Solid Earth 98, 4143–4161.
Hussenoeder, S.A., Collins, J.A., Kent, G.M., Detrick, R.S., Harding, A.J., Orcutt, J.A., Mutter, J.C., Buhl, P., 1996. Seismic analysis of the axial magma chamber reflector along the southern East Pacific Rise from conventional reflection profiling. J. Geophys. Res., Solid Earth 101, 22087–22105.
Katz, R.F., Weatherley, S.M., 2012. Consequences of mantle heterogeneity for melt extraction at mid-ocean ridges. Earth Planet. Sci. Lett. 335, 226–237.
Kelemen, P.B., Aharonov, E., 1998. Periodic formation of magma fractures and generation of layered gabbros in the lower crust beneath oceanic spreading ridges. In: Faulting and Magmatism at Mid-Ocean Ridges. In: Geophysical Monograph Series, vol. 106, pp. 267–289.
Kent, G.M., Harding, A.J., Orcutt, J.A., 1993. Distribution of magma beneath the East Pacific Rise between the Clipperton Transform and the 9°17′N deval from forward modeling of common depth point data. J. Geophys. Res., Solid Earth 98, 13945–13969.
Kent, G.M., Harding, A.J., Orcutt, J.A., Detrick, R.S., Mutter, J.C., Buhl, P., 1994. Uniform accretion of oceanic-crust south of the Garrett Transform at 14°15′S on the East Pacific Rise. J. Geophys. Res., Solid Earth 99, 9097–9116.
Key, K., Constable, S., Liu, L.J., Pommier, A., 2013. Electrical image of passive mantle upwelling beneath the northern East Pacific Rise. Nature 495, 500.
Langmuir, C.H., Bender, J.F., Batiza, R., 1986. Petrological and tectonic segmentation of the East Pacific Rise, 5°30′–14°30′N. Nature 322, 422–429.
Macdonald, K.C., Fox, P.J., Perram, L.J., Eisen, M.F., Haymon, R.M., Miller, S.P., Carbotte, S.M., Cormier, M.H., Shor, A.N., 1988. A new view of the mid-ocean ridge from the behavior of ridge-axis discontinuities. Nature 335, 217–225.
Marjanović, M., 2013. Signatures of present and past melt distribution at fast and intermediate spreading centers. Ph.D. thesis. Department of Earth and Environmental Sciences, Columbia University, New York.
Menand, T., 2008. The mechanics and dynamics of sills in layered elastic rocks and their implications for the growth of laccoliths and other igneous complexes. Earth Planet. Sci. Lett. 267, 93–99.
Menand, T., 2011. Physical controls and depth of emplacement of igneous bodies: A review. Tectonophysics 500, 11–19.
Mutter, J.C., Carton, H.D., 2013. The Mohorovicic discontinuity in ocean basins: Some observations from seismic data. Tectonophysics 609, 314–330.
Mutter, J.C., Carbotte, S., Nedimovic, M., Canales, J.P., Carton, H., 2009. Seismic imaging in three dimensions on the East Pacific Rise. Eos, Trans. Am. Geophys. Union 90, 374–375.
Niu, Y.L., Batiza, R., 1997. Trace element evidence from seamounts for recycled oceanic crust in the eastern Pacific mantle. Earth Planet. Sci. Lett. 148, 471–483.
Niu, Y.L., Regelous, M., Wendt, I.J., Batiza, R., O'Hara, M.J., 2002. Geochemistry of near-EPR seamounts: importance of source vs. process and the origin of enriched mantle component. Earth Planet. Sci. Lett. 199, 327–345.
Parsons, T., Sleep, N.H., Thompson, G.A., 1992. Host rock rheology controls on the emplacement of tabular intrusions – implications for underplating of extending crust. Tectonics 11, 1348–1356.
Perfit, M.R., Fornari, D.J., Smith, M.C., Bender, J.F., Langmuir, C.H., Haymon, R.M., 1994. Small-scale spatial and temporal variations in midocean ridge crest magmatic processes. Geology 22, 375–379.
Phipps Morgan, J., Chen, Y.J., 1993. The genesis of oceanic-crust – magma injection, hydrothermal circulation, and crustal flow. J. Geophys. Res., Solid Earth 98, 6283–6297.
Rubin, K.H., Macdougall, J.D., Perfit, M.R., 1994. Po-210–Pb-210 dating of recent volcanic-eruptions on the sea-floor. Nature 368, 841–844.
Scheirer, D.S., Macdonald, K.C., 1995. Near-axis seamounts on the flanks of the East Pacific Rise, 8°N to 17°N. J. Geophys. Res., Solid Earth 100, 2239–2259.
Shen, Y., Forsyth, D.W., Scheirer, D.S., Macdonald, K.C., 1993. 2 forms of volcanism – implications for mantle flow and off-axis crustal production on the west flank of the southern East Pacific Rise. J. Geophys. Res., Solid Earth 98, 17875–17889.
Sims, K.W.W., Blichert-Toft, J., Fornari, D.J., Perfit, M.R., Goldstein, S.J., Johnson, P., DePaolo, D.J., Hart, S.R., Murrell, P.J., Michael, P.J., Layne, G.D., Ball, L.A., 2003. Aberrant youth: Chemical and isotopic constraints on the origin of off-axis lavas from the East Pacific Rise, 9°–10°N. Geochem. Geophys. Geosyst. 4.
Sleep, N.H., 1975. Formation of oceanic crust – some thermal constraints. J. Geophys. Res. 80, 4037–4042.
Smith, M.C., Perfit, M.R., Fornari, D.J., Ridley, W.I., Edwards, M.H., Kurras, G.J., Von Damm, K.L., 2001. Magmatic processes and segmentation at a fast spreading mid-ocean ridge: Detailed investigation of an axial discontinuity on the East Pacific Rise crest at 9°37′N. Geochem. Geophys. Geosyst. 2.
Sohn, R.A., Sims, K.W.W., 2005. Bending as a mechanism for triggering off-axis volcanism on the East Pacific Rise. Geology 33, 93–96.
Soule, S.A., Fornari, D.J., Perfit, M.R., Rubin, K.H., 2007. New insights into mid-ocean ridge volcanic processes from the 2005–2006 eruption of the East Pacific Rise, 9°46′N–9°56′N. Geology 35, 1079–1082.
Tolstoy, M., Waldhauser, F., Bohnenstiehl, D.R., Weekly, R.T., Kim, W.Y., 2008. Seismic identification of along-axis hydrothermal flow on the East Pacific Rise. Nature 451, 181–187.
Toomey, D.R., Jousselin, D., Dunn, R.A., Wilcock, W.S.D., Detrick, R.S., 2007. Skew of mantle upwelling beneath the East Pacific Rise governs segmentation. Nature 446, 409–414.
Turner, S., Beier, C., Niu, Y., Cook, C., 2011. U–Th–Ra disequilibria and the extent of off-axis volcanism across the East Pacific Rise at 9°30′N, 10°30′N, and 11°20′N. Geochem. Geophys. Geosyst. 12.
Vera, E.E., Mutter, J.C., Buhl, P., Orcutt, J.A., Harding, A.J., Kappus, M.E., Detrick, R.S., Brocher, T.M., 1990. The structure of 0-My to 0.2-My old oceanic-crust at 9°N on the East Pacific Rise from expanded spread profiles. J. Geophys. Res., Solid Earth Planets 95, 15529–15556.
Waters, C.L., Sims, K.W.W., Perfit, M.R., Blichert-Toft, J., Blusztajn, J., 2011. Perspective on the genesis of E-MORB from chemical and isotopic heterogeneity at 9–10°N East Pacific Rise. J. Petrol. 52, 565–602.
White, S.M., Macdonald, K.C., Scheirer, D.S., Cormier, M.H., 1998. Distribution of isolated volcanoes on the flanks of the East Pacific Rise, 15.3°S–20°S. J. Geophys. Res., Solid Earth 103, 30371–30384.
White, S.M., Haymon, R.M., Fornari, D.J., Perfit, M.R., Macdonald, K.C., 2002. Correlation between volcanic and tectonic segmentation of fast-spreading ridges: Evidence from volcanic structures and lava flow morphology on the East Pacific Rise at 9°–10°N. J. Geophys. Res., Solid Earth 107.
White, S.M., Haymon, R.M., Carbotte, S., 2006. A new view of ridge segmentation and near-axis volcanism at the East Pacific Rise, 8°–12°N, from EM300 multibeam bathymetry. Geochem. Geophys. Geosyst. 7.
Wilcock, W.S.D., Solomon, S.C., Purdy, G.M., Toomey, D.R., 1995. Seismic attenuation structure of the East Pacific Rise near 9°30′N. J. Geophys. Res., Solid Earth 100, 24147–24165.
Zindler, A., Hart, S., 1986. Chemical geodynamics. Annu. Rev. Earth Planet. Sci. 14, 493–571.
Zindler, A., Staudigel, H., Batiza, R., 1984. Isotope and trace-element geochemistry of young pacific seamounts – implications for the scale of upper mantle heterogeneity. Earth Planet. Sci. Lett. 70, 175–195.
Zou, H.B., Zindler, A., Niu, Y.L., 2002. Constraints on melt movement beneath the East Pacific Rise from Th-230–U-238 disequilibrium. Science 295, 107–110.